Quantifying the effect of off-focal radiation on the output of kilovoltage x-ray systems

E. S. M. Ali[a] and D. W. O. Rogers[b]
Carleton Laboratory for Radiotherapy Physics, Ottawa Carleton Institute for Physics, Carleton University, 1125 Colonel By Drive, Ottawa, Ontario K1S 5B6, Canada

(Received 14 January 2008; revised 9 July 2008; accepted for publication 10 July 2008; published 20 August 2008)

In a typical x-ray tube, off-focal radiation is mainly generated by the backscattered electrons that reenter the anode outside the focal spot. In this study, BEAMnrc (an EGSnrc user-code) is modified to simulate off-focal radiation. The modified BEAMnrc code is used to study the characteristics of electrons that backscatter from the anode, and to quantify their effect on the output of typical x-ray systems. Results show that the first generation backscatter coefficient is ~50% for tungsten anodes at diagnostic energies, and ~38% for molybdenum anodes at mammography energies. Second and higher generations of backscatter have a relatively minor contribution. At the patient plane, our simulation results are in excellent agreement with experimental measurements in the literature for the spectral shape of both the primary and the off-focal components, and also for the integral off-focal-to-primary ratio. The spectrum of the off-focal component at the patient plane is softer than the primary, which causes a slight softening in the overall spectrum. For typical x-ray systems, the off-focal component increases patient exposure (for a given number of incident primary electrons) by up to 11% and reduces the half-value layer and the effective energy of the average spectrum by up to 7% and 3%, respectively. The larger effects are for grounded cathode tubes, smaller interelectrode distance, higher tube voltage, lighter filtration, and less collimation. Simulation time increases by ~30% when the off-focal radiation is included, but the overall simulation time remains of the order of a few minutes. This study concludes that the off-focal radiation can have a non-negligible effect on the output parameters of x-ray systems and that it should be included in x-ray tube simulations for more realistic modeling of these systems. [DOI: 10.1118/1.2966348]

Key words: off-focal radiation, extra-focal radiation, electron backscatter, x-ray tubes, EGSnrc, BEAMnrc, Monte Carlo simulations

I. INTRODUCTION

In a typical x-ray tube, when the focal spot is blocked and a projection image of the anode is taken, many parts of the anode can still be seen in the image.[1] This suggests the presence of a radiation source located "off" the focal spot, and this radiation is aptly named the "off-focal" radiation. The presence of an off-focal component in the overall output of an x-ray system has been known since the early days of x-ray tubes. It has also been called secondary,[2] stray,[3] parasitic,[4] extra-focal[5–7] and off-focus radiation.[8–10] Off-focal radiation is mainly due to the large fraction of electrons that backscatter out of the anode into the tube vacuum, then accelerate back towards the anode under the influence of the interelectrode electric field. These backscattered electrons reenter the anode mostly outside the focal spot and interact with the anode material to produce the bremsstrahlung and characteristic radiation that makes up most of the off-focal component. Electric field distortions and the design of the focusing cup cause some of the primary electrons to be misfocused; these misfocused electrons also contribute to the off-focal component in x-ray systems. However, it has been reported[11,12] that the contribution of misfocused electrons to the off-focal component is minor compared to that of electrons backscattered from the anode surface. The undesirable effects of the off-focal radiation, and the various methods to reduce it in x-ray systems have been discussed in the literature.[3–22] To date, there has been no practical way to completely eliminate the off-focal component because it is generated *inside* the vacuum envelope of the x-ray tube. Thus, off-focal radiation due to backscattered electrons is an inherent component of the output of x-ray systems, including modern ones.[21,22]

Over the years, there have been experimental[1–4,13–16,20–23] and computational[15,20,21,24,25] efforts to quantify the magnitude and effect of the off-focal component on x-ray systems. Since there is no standardized method to experimentally measure the off-focal component,[12] the experimental results vary dramatically depending on the measurement technique. For example, Kuhn and Gajewski[5] reported that the ratio of the exposure due to the off-focal component to the exposure due to the primary component is 5%, 20%, or 25% for *the same* tube assembly using three different measurement techniques. In addition, in many investigations, only the qualitative effects of the off-focal component on the radiographs are reported. The very few computational efforts are specific in scope; Rao[15] mainly focused on an analytical derivation for the effect of the off-focal component on the modulation transfer function. In the context of x-ray fluorescence analysis, Pavlinsky and Portnoy[24,25] focused on the effect of the off-focal component on the characteristic peaks of the x-ray spectrum depending on the type of grounding of the tube. Wen *et al.*[20,21] focused on the effect of the off-focal radiation on the output of an x-ray tube when placed in the magnetic field of an MR scanner in a hybrid CT/MRI system. To the authors' knowledge, there have not been any computational studies (Monte Carlo or otherwise) that fully characterized the source and effect of off-focal radiation for a series of tube arrangements typical in mammography, diagnostic, and orthovoltage applications. The goal of this study is to fill this gap in the computational study of the origin and effect of off-focal radiation, and to provide a simulation tool that includes the off-focal component for more realistic, and yet efficient and user-friendly, modeling of x-ray systems.

In this study, BEAMnrc[26,27] (an EGSnrc[28,29] user-code) is used. Because off-focal radiation is a direct result of electron backscatter, it was essential to first investigate the accuracy of the EGSnrc/BEAMnrc system in performing backscatter calculations. This investigation was done in two recent studies[30,31] in which we showed that, for the energy range of interest to x-ray tube operation, there is excellent agreement between EGSnrc charged particle backscatter calculations and most of the experimental measurements from 31 different experiments. The reader is referred to the two papers for the details of the exhaustive comparisons, and for a discussion of the uncertainties and potential limitations of EGSnrc in performing charged particle backscatter calculations.

In the current study, BEAMnrc is modified to include electron transport in an electric field in vacuum in order to properly transport backscattered electrons into the anode. The modified BEAMnrc code is used to study the characteristics of the backscattered electrons that cause the off-focal radiation. This includes backscatter coefficients, energy spectra, angular distributions, and spread functions of all generations of backscattered electrons. Next, typical arrangements of mammography, diagnostic, and orthovoltage x-ray systems are simulated, and the effect of the off-focal component on the system output is quantified for typical ranges of operational parameters (tube voltage and filtration). Our simulation results are compared with experimental measurements available in the literature for a diagnostic system[6] and for a digital mammography system,[22] and also compared with results from theoretical models.[24]

II. METHODS

II.A. Considerations in anode simulation

Off-focal radiation is more important for rotating anode tubes than it is for stationary anode tubes for two reasons. First, a rotating anode has a larger disk, which increases the probability that backscattered electrons reenter the anode. Second, the bulk of a rotating anode disk is made of a material (typically tungsten or molybdenum) of higher Z than the material that makes up the bulk of a stationary anode (typically copper). A higher-Z material surrounding the focal spot means a higher probability that the backscattered electrons generate off-focal bremsstrahlung upon reentering the anode outside the focal spot. Off-focal radiation is also more important for grounded cathode tubes than it is for grounded anode tubes.[19] For grounded anode tubes, the anode is at the same potential as its surroundings and, thus, backscattered electrons are not particularly attracted to the anode. Conversely, for grounded cathode tubes, the anode is at high positive potential relative to its surroundings and, thus, backscattered electrons are strongly attracted to the anode. This study illustrates the off-focal radiation effects for grounded cathode rotating anode tubes as an extreme case. Center-tapped tubes, which are commonly used in diagnostic imaging, would have an off-focal component somewhere between that for grounded cathode tubes and that for grounded anode ones.

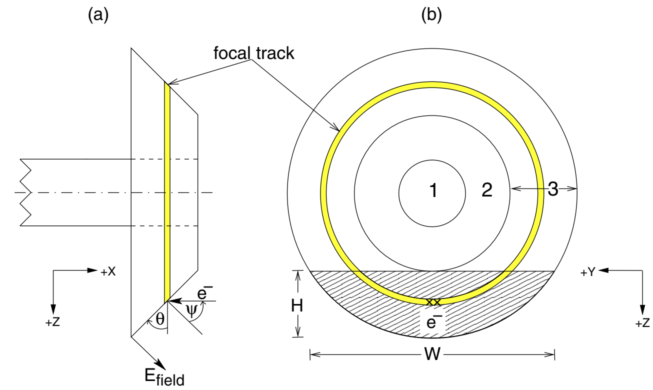

FIG. 1. Two views of the geometry of a typical rotating anode. See section II.A. for discussion. xx marks the focal spot. Regions 1, 2, and 3 are the anode stem, disk face, and tilted surface, respectively.

In our analysis, a number of simplifying assumptions are used in order to be able to tackle the problem mathematically. (1) It is known that close to the surface of a conductor, the electric field is perpendicular to the conductor surface.[32] The assumption we made is that, to first order, the field remains perpendicular to the conducting anode surface throughout the interelectrode space. Some tube designs have the cathode tilted to be parallel to the focal spot,[33] and the electric field is almost exactly perpendicular to the anode surface throughout the interelectrode space (except for the edge effects). (2) Local and temporal distortions in the electric field are ignored, i.e., the field is assumed to be uniform and constant. (3) The generation of a large number of backscattered electrons over the anode surface (similar, in a sense, to the well-known space-charge effect at the cathode filament) is assumed not to disturb the electric field. (4) Radiation damping—by which backscattered electrons lose energy in the form of bremsstrahlung due to their acceleration and deceleration in the electric field—is ignored because it has been shown[34] to be negligible.

Figure 1 shows two views of the geometry of a typical rotating anode. The x rays generated by backscattered electrons that reenter the anode stem (region 1), disk face (region 2), or the non-hatched area of the tilted surface (region 3) hardly contribute to the off-focal radiation at the patient plane because they are either directed away from the plane, i.e., geometric constraints, or, if they are directed towards it, are unlikely to penetrate the very thick high-Z material in the +Z direction. Therefore, the only area simulated in this study is the hatched area. In BEAMnrc, the module simulating an x-ray anode handles only rectilinear objects, therefore, the curved hatched area is approximated with a rectangular one of the same width and height ($W \simeq 10$ cm and $H \simeq 2.5$ cm for a typical rotating anode). Our sensitivity analysis and the excellent agreement with experimental measurements (shown later) both confirm that the approximate geometry just presented is reasonable, and that it scopes most of the off-focal radiation effects.

As the primary electrons accelerate from the cathode towards the anode, their trajectories are bent in order to follow the electric field lines, which are perpendicular to the conducting anode close to the surface as discussed above. Therefore, the exact angle of entry into the anode [ψ in Fig. 1(a)] is somewhere between zero (i.e., perpendicular incidence) and θ (the anode tilt angle). Finite element simulations suggest that primary electrons enter the anode normally or near normally.[19,35] In addition, it has been shown both experimentally and by Monte Carlo simulations that when ψ changes from zero up to 30°, the fraction of primary electrons that backscatter from a high-Z target increases by no more than 2% (see Fig. 4 in Ref. 30). All this means that for the purpose of studying off-focal radiation (which is mainly due to backscattered electrons), the exact angle of entry of the primary electrons (ψ) is not critical for as long as it remains below ~30°.

The mathematical analysis developed in this study requires a knowledge of the interelectrode distance d. Our survey of medical x-ray tube inserts shows that d varies from ~1 cm to ~4.5 cm with a typical value of ~1.5 cm, which is used in the simulations throughout this study. The effects of d on the off-focal component is discussed in Sec. III C.

Simulations in this study are done for pencil beams of primary electrons incident on point-like focal spots and for anode disks made of the same materials as the focal tracks. The variation of the off-focal component with the focal spot size and the effect of the anode disk material being different from the focal track material are both discussed in Sec. III C.

Finally, we assumed that backscattered electrons do not hit the cathode along their trajectories in the tube vacuum. This is based on the simple energy conservation argument that the most energetic backscattered electrons can move a perpendicular distance from the anode surface no larger than the interelectrode distance d. Further, as will be seen in Sec. III A, backscattered electrons reach the peak of their trajectories away from the cathode-anode line, not directly where the cathode is.

II.B. Modifying BEAMnrc

To add to BEAMnrc the ability to simulate off-focal radiation, the code is modified to include electron transport in an electric field in vacuum (the EM macros by Bielajew[36] are compatible with EGS4[37] not EGSnrc[28,29]). The EGSnrc electron transport *inside* the anode is not altered by the presence of the interelectrode electric field. This is because the conducting anode material requires a vanishingly small electric field to drive a current, therefore the electric field can safely be taken as zero inside the anode even though a tube current is flowing[32] (much like assuming an electric wire to be equipotential even though a current is flowing in the circuit). The appendix at the end of this paper presents a brief description of the mathematical model used in the implementation, and the algorithm used to determine the energy, location, and direction of reentry of the backscattered electrons. The implementation also takes into account that electrons can backscatter multiple times. The convention used in this study is that when a primary electron backscatters, it belongs to the *first generation* of backscatter. When one of the first generation backscattered electrons reenters the anode and then backscatters again, it belongs to the *second generation* of backscatter. Backscattering more than twice generates *higher generations* of backscattered electrons.

One of the diagnostic tubes simulated in our study[6] is a 12-pulse tube with a voltage ripple factor of ~5%. To include this ripple effect, BEAMnrc is modified to generate the proper incident primary electron spectrum. The spectrum is generated by uniformly sampling points in time and calculating the corresponding tube voltages, and then binning the calculated voltage values to create the spectrum. Next, every bin value in the spectrum is weighted by its corresponding voltage, i.e., the number of primary electrons incident on the anode is assumed to be proportional to the tube voltage for a given filament current, which is a reasonable assumption for small ripple factors. A more rigorous approach is to use the voltage/current (V/I) characteristic curve of the simulated tube to assign weights to the bin values of the electron spectrum. However, this is not adopted in our study because the V/I curve for the tube under consideration is not available, and also because our simulation results show that a 5% ripple factor has a minor effect on the study of off-focal radiation.

II.C. Simulation of typical x-ray systems

To get a realistic sense of the extent of the off-focal component, typical x-ray systems used in mammography, diagnostic and orthovoltage applications are simulated. The representative diagnostic system used in this study has a 16° tungsten/rhenium (90/10) rotating anode. Inherent and added filtration are 0.5 and 2.0 mm aluminum equivalent, respectively. Primary collimation of 1 cm thick lead plates is placed immediately outside the tube exit window (~3 cm from the focal spot) such that it creates a field of view of 56 cm diameter at 100 cm SSD. Secondary collimation is placed at 15 cm to create a 20×20 cm^2 diagnostic field at 100 cm SSD. The representative mammography system has a 10° molybdenum rotating anode, a 30 μm molybdenum filter and secondary collimation to create an 18×18 cm^2 field at 65 cm SSD. The representative orthovoltage system has a 24° tungsten/rhenium (90/10) rotating anode, a filter of 0.5 mm copper, followed by 2 mm aluminum, and an applicator to create a 10×10 cm^2 therapeutic field at 52 cm SSD.

The representative operating voltages are 26, 100, and 250 kV for the mammography, diagnostic, and orthovoltage systems, respectively.

For comparison with experimental measurements, we simulated the diagnostic system used in the measurements by Birch[6] and the SenoScan® digital mammography system[38,39] used in the measurements by Shen *et al.*[22] Birch[6] used a 12-pulse diagnostic system with a 10° rotating-anode tungsten target and a total filtration of 2 mm aluminum. The pinhole configuration allowed for 5.4 mm^2 of the anode surface to be seen by a Ge(Li) detector. The pinhole center was aligned with the center of the focal spot to measure the primary spectrum, then the pinhole configuration was shifted 3.5–4.0 mm off the focal spot center to measure the off-focal spectrum. Measurements were made at kVps of 50 and 100. Shen *et al.*[22] measured the exposure (or air kerma) due to the off-focal component relative to that due to the primary for the SenoScan® digital mammography system. The tube had a 7° tungsten/rhenium target and the total filtration was 2.5 mm aluminum. Collimation was such that it created a $1.14 \times 23\ cm^2$ scanning slot at 65 cm SSD. The primary component was measured using central pinhole configuration, and the off-focal component was measured by blocking the focal spot in an open field. Measurements were made for tube voltages between 26 and 40 kV in 1 kV increments.

In all simulations performed in our study, photons and electrons are tracked down to a kinetic energy of 1 keV. The most accurate low-energy physics[29] and cross-section data[40–42] available in EGSnrc are employed. A value of 5×10^{-7} cm is used for the BEAMnrc internal parameter $BDY_TOL. The reader is referred to Ref. 30 for a full discussion of the effect of this parameter on the accuracy of BEAMnrc charged particle backscatter calculations. The simulation CPU time increases by ~30%, 45%, and 55% when first, first+second, and all generations of backscattered electrons are included, respectively. However, simulations remain fast because the variance reduction techniques available in BEAMnrc for kilovoltage x-ray simulations are employed.[43–45] When only the primary or the total output are of interest, typical CPU simulation times are of the order of a few minutes on a single 3.0 GHz Intel-® Woodcrest 64-bit processor. Simulation times are extended to a few hours when very good statistics are sought on the off-focal component.

To analyze the output of the simulated x-ray systems, four metrics are used in this study: the spectral shape, the air kerma at the patient plane per incident primary electron (K_{air}), the half-value layer (HVL), and the spectrum effective energy (E_{eff}). For spectral shapes, the spectra are averaged over the diagnostic or therapeutic field of interest and arbitrarily normalized to unity at their bremsstrahlung peaks. K_{air} is determined by summing the bin values of the energy fluence spectrum at the patient plane weighted by their respective mass energy absorption coefficients for air. The HVL is determined by iterating the absorber thickness until the air kerma reaches half its value without the absorber. Finally, E_{eff} is the energy of a monoenergetic x-ray beam that has the same HVL as the spectrum of interest.

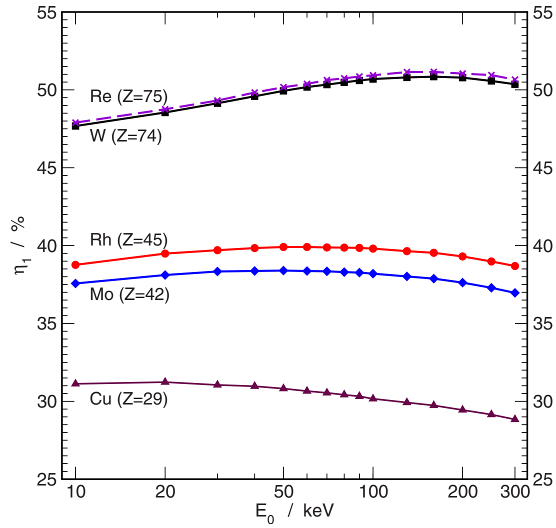

FIG. 2. Calculated first generation electron backscatter coefficient (η_1) for elements used in typical anode alloys. The incident electron beam energy E_0 goes from the mammography to the orthovoltage range. The scale of the abscissa is logarithmic.

III. RESULTS AND DISCUSSION

III.A. Characteristics of electrons backscattering from the anode

The results presented in this section include backscatter coefficients, energy spectra, angular distributions, and spread functions for multiple generations of electrons that backscatter from the anode in typical mammography, diagnostic, and orthovoltage systems. No comparisons with experimental measurements are presented in this section because an exhaustive benchmark against 31 different experiments has been reported previously.[30,31] The systematic and statistical uncertainties in the EGSnrc/BEAMnrc simulations are estimated to be ≤3% and ≤1%, respectively, and they are not shown for clarity of the graphs. The reader is referred to Refs. 30 and 31 for the justification of these uncertainties.

The electron backscatter coefficient η is the number of electrons with kinetic energy >1 keV that backscatter out of the anode divided by the number of incident primary electrons. Figure 2 shows the calculated first generation electron backscatter coefficient (η_1) for elements used in typical anode alloys. For the energy range of interest to x-ray tube operation, η_1 is almost energy independent. As Z increases, η_1 increases, which indicates that the off-focal component at the patient plane is expected to be larger for higher-Z anodes. The value of η_1 is ~50% for tungsten anodes at diagnostic energies, and ~38% for molybdenum anodes at mammography energies. Rhenium, which is typically added to tungsten for strength, has a value of η_1 very similar to that of tungsten; therefore, the off-focal components with and without rhenium are virtually the same.

TABLE I. Calculated electron backscatter coefficient (η) for multiple generations of backscatter in typical x-ray anodes.

Simulation case	Electron Backscatter Coefficient / %			
	first (η_1)	second (η_2)	>second ($\eta_{>2}$)	Total
Mammography, Mo, 26 kV	37.6	11.7	6.5	55.8
Diagnostic, W, 100 kV	50.6	18.1	13.8	82.5
Orthovoltage, W, 250 kV	50.6	19.1	15.7	85.4

Our simulation results show that η_1 includes $\leqslant 1\%$ contribution from backscattered non-primary electrons, i.e., electrons created in Moller interactions, photoelectrons, Compton scatter electrons, and Auger electrons. The contribution of secondary electrons is very small because[30,31] there are not many of them created by the primaries near the surface. In addition, secondary electrons typically have very low energies and they are likely to stop in the anode material before backscattering into the tube vacuum.

Table I shows η for multiple generations of backscatter. Because η is almost energy independent, when a fraction f backscatters for the first time, roughly f of it is expected to backscatter a second time, and so on. This implies that the backscatter between successive generations is expected to *loosely* follow a geometric series with a sum of $f/(1-f)$. This can be seen in the values of the total in Table I—e.g., the total for the mammography anode (55.8%) is close to $0.376/(1-0.376)=60\%$. The values of η_2 and $\eta_{>2}$ do not include the contribution from first generation electrons that land outside the anode area of width W and height H [Fig. 1(b)].

Although EGSnrc/BEAMnrc simulation results of η_1 have been extensively compared with experimental measurements,[30] there are no experimental measurements available for the higher generations of backscatter. The only data we could locate are those calculated by Pavlinsky and Portnoy[24] using an analytical model, which gives $\eta_2=7.5\%$, 16.4%, and 23.5% for 40 keV primary electrons incident on chromium, rhodium, and tungsten, respectively; our corresponding simulation values are 10.7%, 20.1%, and 28.8%, respectively.

Figure 3 shows the calculated energy spectra of backscattered electrons. Panel a shows that first generation backscattered electrons retain a large fraction of their original energy, and the fraction increases as Z increases. This is because electrons mostly undergo a few large-angle elastic scattering deflections before they backscatter, with larger deflection angles and fewer inelastic collisions as Z increases. Panel b shows that the energy spectra dramatically shift towards lower energies from one generation to the next. This implies that higher generations of backscattered electrons have a minor impact on the overall off-focal component at the patient plane because they are fewer in number (Table I) and lower in energy [Fig. 3(b)]; therefore, they only generate a small number of low-energy off-focal x rays, which will unlikely escape the anode self-filtration. Previously, we have reported[31] many comparisons between experimental measurements and EGSnrc/BEAMnrc simulation results for the energy spectra of the first generation of electrons backscattered from different solid targets. However, the only data we could locate for the energy spectra of the second generation of backscatter are those calculated by Pavlinsky and Portnoy[24] using an analytical model, and they are shown in Fig. 4. The spectra in Figs. 3 and 4 are plotted starting at $E/E_0=0.1$ because the data at lower energies are less reliable—see Refs. 30 and 31 for a discussion of the potential limitations of EGSnrc at very low energies.

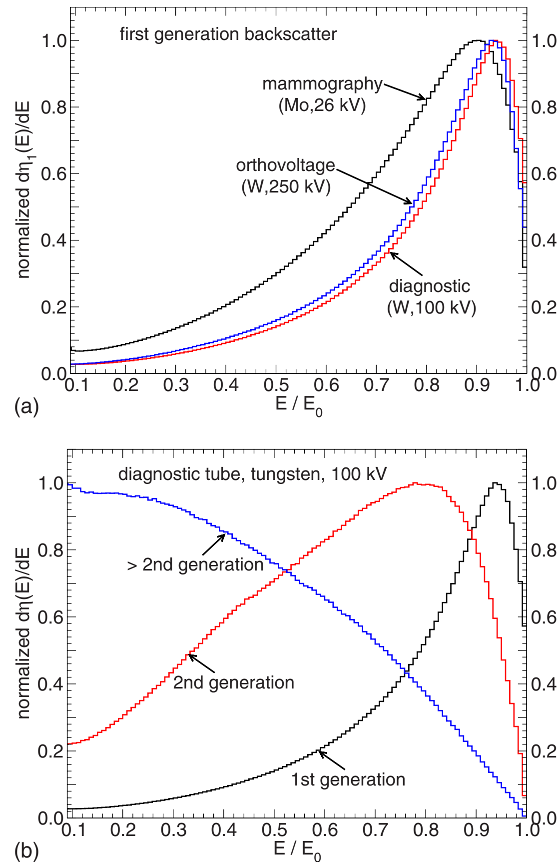

FIG. 3. Calculated energy spectra of electrons backscattered at all angles from typical x-ray anodes. Panel a: first generation backscatter, panel b: multiple generations. All curves are arbitrarily normalized to unity at their peaks. E_0 and E are the kinetic energies of the incident and backscattered electrons, respectively. $d\eta(E)$ is the number of electrons that backscatter from the anode surface with energy between E and $E+dE$.

Figure 5 shows the calculated angular distributions of backscattered electrons. Panel a shows that the most probable angle of backscattering is $\sim 45°$ relative to the anode surface, i.e., $\sim 135°$ relative to the original direction of incidence. To get the angular distributions differential in the solid angle (Ω) as opposed to the angle (α), the distributions shown should be divided by $4\pi \sin(90°-\alpha)$, in which case the resulting distributions would peak at $\alpha=90°$, similar to the experimental and Monte Carlo results reported previously.[31] For higher generations (panel b), the angular

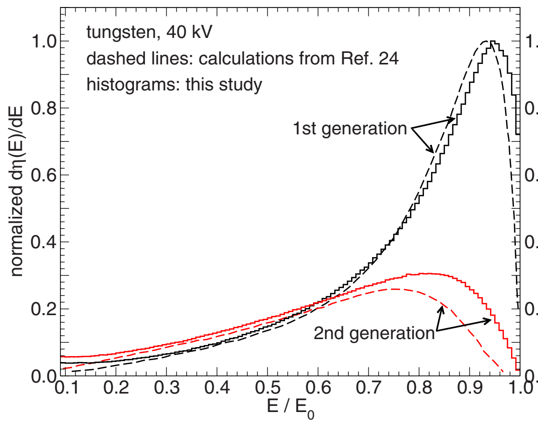

FIG. 4. Comparison between our simulation results and the results calculated by Pavlinsky and Portnoy (Ref. 24) for the energy spectra of first and second generations of backscattered electrons in a tungsten anode. Parameters are defined as in Fig. 3.

distribution preserves its shape with some shift from one generation to the next towards shallower backscatter angles with respect to the anode surface.

Figure 6 shows the calculated spread functions of backscattered electrons (i.e., how far backscattered electrons spread around the center of the focal spot). Panel a shows that the first generation backscattered electrons undergo almost the same spread around the focal spot (i.e., up to $\sim$3 cm), regardless of the tube voltage. This is because the spread functions depend on the *ratio* of the kinetic energy of the backscattered electron relative to that of the primary (E/E_0), not on E alone [see the nonrelativistic form of Eq. (A7) in the Appendix]. Panel a shows that the exact dimensions of the anode beyond a $\sim$3 cm radius around the focal spot are not critical for the purposes of studying the off-focal component, which justifies our choice of the values of W and H as discussed in Sec. II A. Panel b shows that the higher generations of backscattered electrons spread farther away from the focal spot than the first generation, which is another reason (i.e., geometric constraints) for their minor effect on the overall off-focal component at the patient plane; the other reasons are their being fewer in number and lower in energy as discussed above.

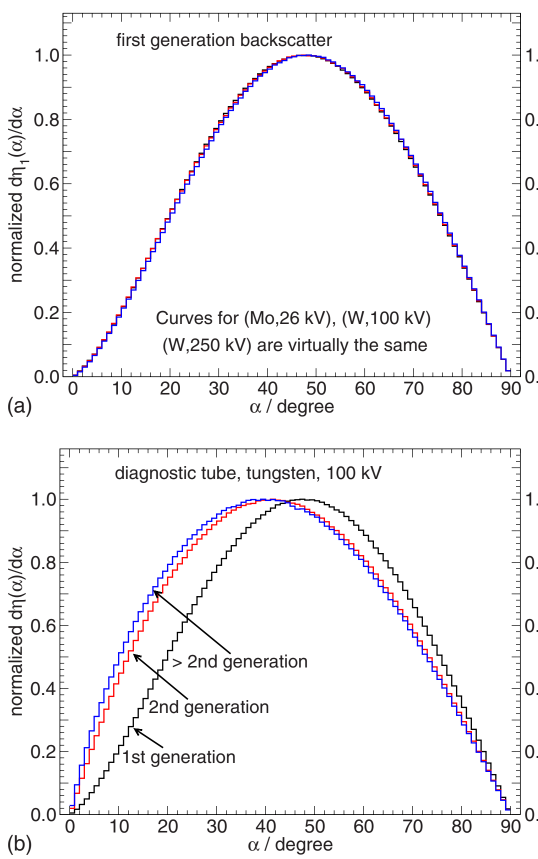

FIG. 5. Calculated angular distributions for electrons backscattered from typical x-ray anodes. Panel a: first generation backscatter, panel b: multiple generations. All curves are arbitrarily normalized to unity at their peaks. α is the backscatter angle *relative to the anode surface* as shown in Fig. 12 in the Appendix. $d\eta(\alpha)$ is the number of electrons backscattered at an angle between α and $\alpha+d\alpha$.

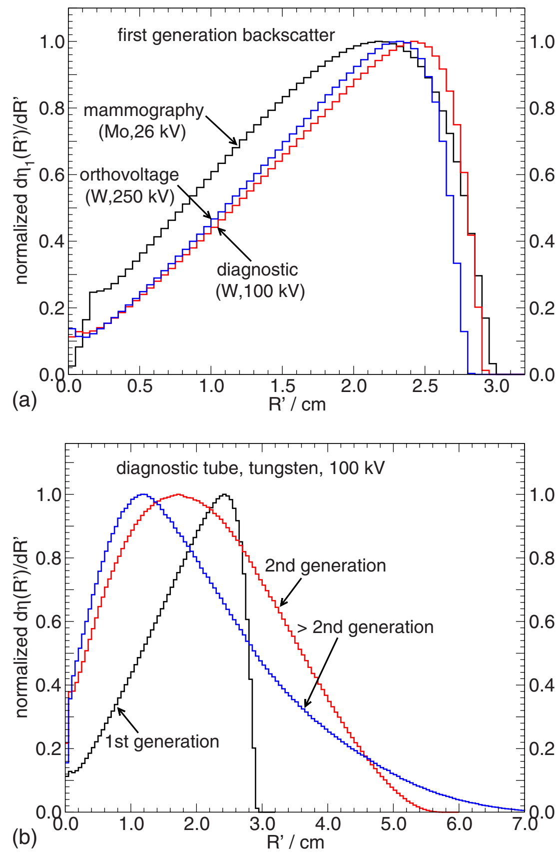

FIG. 6. Calculated spread functions of electrons backscattered from typical x-ray anodes. Panel a: first generation backscatter, panel b: multiple generations. All curves are arbitrarily normalized to unity at their peaks. R' is the distance between the reentry location and the center of the focal spot as shown in Fig. 12 in the Appendix. $d\eta(R')$ is the number of backscattered electrons that reenter the anode between R' and $R'+dR'$.

III.B. Off-focal radiation at the patient plane

This section presents the effects of electrons that backscatter from the anode on the output of typical x-ray systems

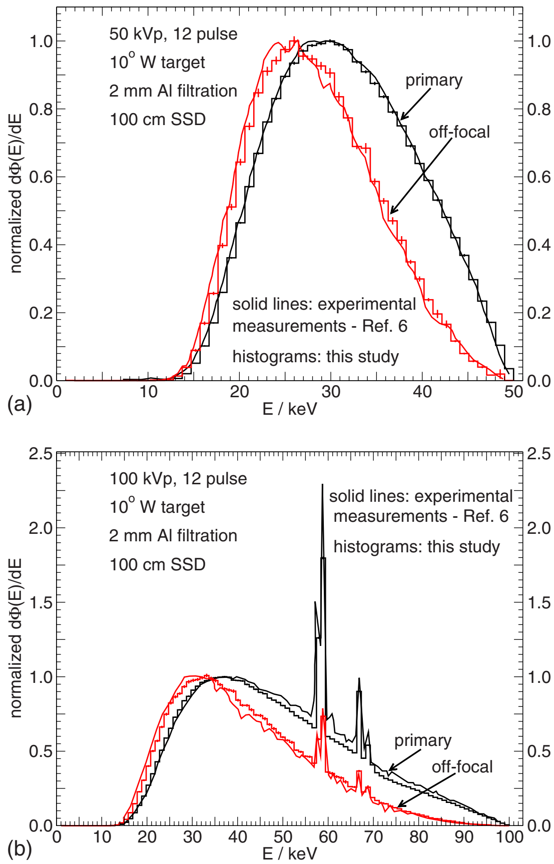

FIG. 7. Comparison between our simulation results and the experimental measurements by Birch (Ref. 6) for the spectral shape of the primary and the off-focal components. All curves are arbitrarily normalized to unity at their bremsstrahlung peaks. Error bars on the simulation histograms of the primary are too small to be seen. E is the photon energy and $d\Phi(E)$ is the number of photons reaching the scoring plane with energy between E and $E+dE$.

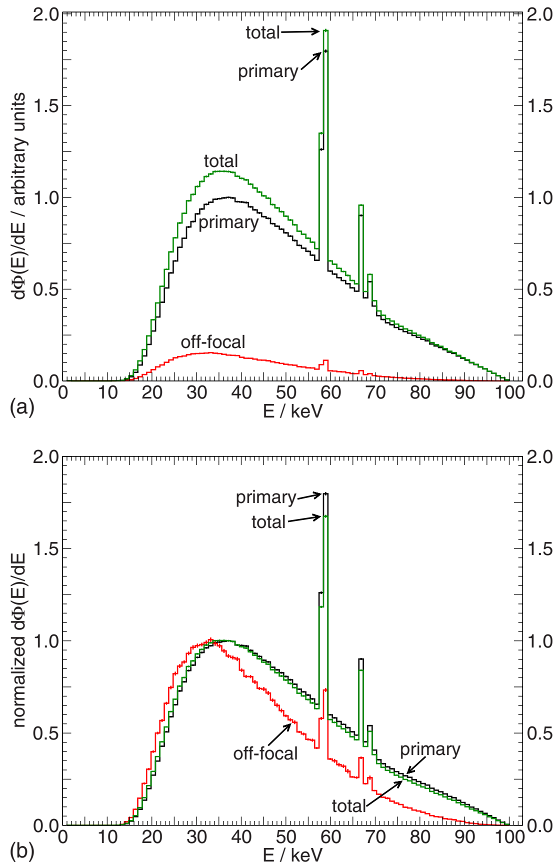

FIG. 8. Simulation results for the effect of the off-focal component on the overall spectral shape for the diagnostic tube described in Fig. 7(b). Panel a: magnitude is included, panel b: only shapes are compared by arbitrarily normalizing all spectra to unity at their bremsstrahlung peaks. Parameters are defined as in Fig. 7. Note that the ordinate labels in a and b are different. Most of the error bars on the simulation histograms are too small to be seen.

at the patient plane. The effects are expressed in terms of variations in the spectral shape, $K_{\rm air}$, HVL, and $E_{\rm eff}$ as defined in Sec. II C.

Figure 7 shows a comparison between our simulation results and the experimental measurements by Birch[6] for both the primary and the off-focal spectra. The overall agreement is excellent except for the discrepancy in the K_α characteristic peaks in panel b, which is mostly a bin-size artifact because the areas under the experimental and computed peaks are within 10% of each other. The roughness of the experimental spectra could be an artifact of stripping the true spectrum from the detector response, or it could be due to random contributions from parts of the experimental setup other than the anode disk. The agreement in Fig. 7 validates our implementation of off-focal radiation in BEAMnrc. Figure 7 also shows that the off-focal spectrum is softer than the primary, which has been supported by all experimental investigations, except for an isolated case in the earlier days of x-ray tubes when the off-focal component was thought to be more penetrating.[4]

Figure 8(a) shows that for a given number of incident primary electrons, the *total* output of the x-ray system increases because of the off-focal component. When only the *shapes* of the same spectra are compared (panel b), the softer off-focal component causes some softening in the overall spectrum. The intensity of the characteristic peaks is *reduced* if the peaks are at the higher end of the spectrum (e.g., the tungsten K_α and K_β peaks in panel b) and *increased* if the peaks are at the lower end of the spectrum (e.g., the L-shell lines in an unfiltered tungsten spectrum—not shown). The same arguments apply to the characteristic peaks of mammography targets (not shown), depending on the position of the peaks in the spectrum.

In the context of x-ray fluorescence analysis, Pavlinsky and Portnoy[24] used an analytical model to quantify the change in the characteristic peaks due to the presence of an off-focal component. They considered the output of grounded cathode and grounded anode tubes to be a measure of the total response with and without off-focal radiation, respectively. When we simulated the same cases, an overall good agreement is found between the results of the two studies as shown in Table II.

Figure 9 shows the variation of the off-focal component with tube voltage for the representative diagnostic system described in Sec. II C when only the inherent filtration is included and without secondary collimation.

TABLE II. Comparison between our simulation results and the results calculated by Pavlinsky and Portnoy (Ref. 24) for the ratio of the intensity of the characteristic peaks with-to-without the off-focal component. Simulations with and without the off-focal component are done for the same number of incident primary electrons, therefore, the ratio must be ⩾1.00. The ratio includes both bremsstrahlung and relaxation photons at the characteristic energy.

	Model in Ref. 24			This study		
Voltage (kV)	20	40	60	20	40	60
Cr (K_α)	1.13	1.16	1.18	1.12	1.15	1.16
Rh (K_α)	—	1.15	1.22	—	1.14	1.21
Rh (L_α)	1.32	1.40	1.45	1.29	1.37	1.44
W (L_α)	1.26	1.41	1.48	1.27	1.38	1.43

$\Delta K_{\mathrm{air}}/(K_{\mathrm{air}})_{\mathrm{primary}}$ increases with tube voltage by up to 11% because the average energy of the generated off-focal x rays increases with tube voltage, and consequently the probability that they survive the anode self-filtration increases. The same behavior of the relative change in K_{air} versus tube voltage has been observed experimentally.[6,9,15] The range of increase in K_{air} due to the off-focal component is consistent with the 5–25% range reported in different experiments and review articles[1,3,5,6,8,10,14–16,20–23,46,47] depending on the tube design, operating parameters, and measurement technique. Figure 9 also shows that the presence of an off-focal component causes a reduction in $\Delta\mathrm{HVL}/(\mathrm{HVL})_{\mathrm{primary}}$ and $\Delta E_{\mathrm{eff}}/(E_{\mathrm{eff}})_{\mathrm{primary}}$ of up to 7% and 3%, respectively.

In the mammography range, Fig. 10 shows a comparison between our simulation results and the experimental measurements by Shen *et al.*[22] for the air kerma due to the off-focal component relative to that due to the primary in the SenoScan® digital mammography system. The agreement of our simulation results with experimental measurements is excellent given the scatter of the experimental data, which is another validation of our implementation of off-focal radiation in BEAMnrc. The behavior of the relative change in K_{air} versus tube voltage in the mammography range is similar to that observed in Fig. 9. Figure 10 shows that even in modern x-ray systems, off-focal radiation is a non-negligible component of the overall output (up to 5.5% for this particular mammography system).

Figure 11 shows the variation of the off-focal component with total filtration for the representative diagnostic (panel a) and orthovoltage (panel b) systems described in Sec. II C with both the primary and the secondary collimation in place. As the filter thickness increases, the softer off-focal x rays are preferentially absorbed compared to the primaries; consequently, the fractional off-focal component at the patient plane decreases. The same behavior of the off-focal component with filtration has been observed experimentally.[23]

III.C. Discussion

The spectra in this study are averaged over typical field sizes of interest clinically. However, our simulations show that the ratio of the mean energy of the spectrum of a typical x-ray system at the patient plane with-to-without the off-focal component remains constant across the diagnostic or therapeutic field, both in the direction parallel to the anode axis (where the heel effect is observed) and in the perpen-

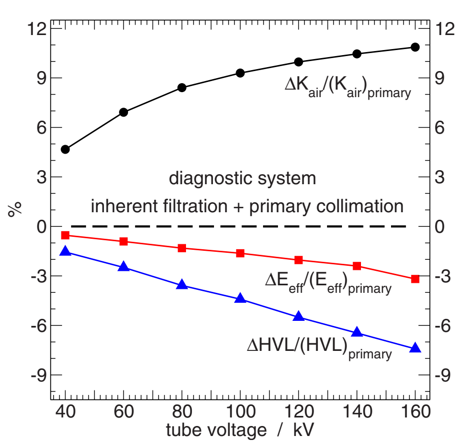

FIG. 9. Simulation results for the variation of the off-focal component with tube voltage for a typical diagnostic system. K_{air} is the air kerma at the patient plane per incident primary electron, HVL is the half-value layer, and E_{eff} is the effective energy of the output spectrum. Spectra are averaged over a $20\times 20\ \mathrm{cm}^2$ diagnostic field at 100 cm SSD.

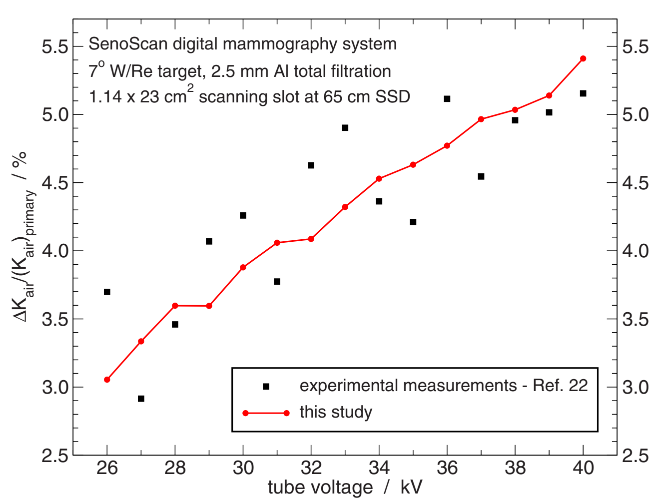

FIG. 10. Comparison between our simulation results and the experimental measurements by Shen *et al.* (Ref. 22) for the magnitude of the off-focal component relative to the primary over the typical voltage range of the SenoScan® digital mammography system (Refs. 38 and 39).

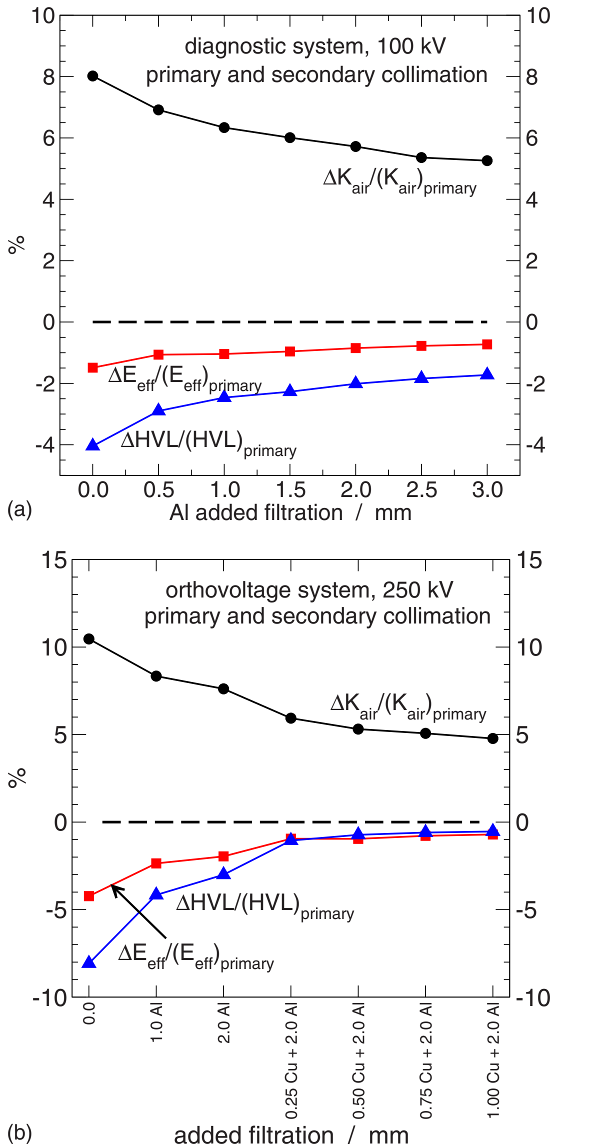

FIG. 11. Simulation results for the variation of the fractional off-focal component with total filtration for typical diagnostic (panel a) and orthovoltage (panel b) systems. Parameters are defined as in Fig. 9. Spectra are averaged over a $20\times 20\,\text{cm}^2$ diagnostic field at 100 cm SSD in panel a, and over a $10\times 10\,\text{cm}^2$ therapeutic field at 52 cm SSD in panel b.

dicular direction. Therefore, the findings of this study also apply to the spectra measured only around the central axis in an open field or around the edges of the field. On the other hand, the off-focal component is expected to be much less for full pinhole configurations because geometric constraints prevent most of the generated off-focal x rays from reaching the very small detector surface.

The value of the interelectrode distance d affects the characteristics of backscattered electrons and consequently the magnitude of the off-focal component at the patient plane as follows. For a given kVp, the spread of first generation backscattered electrons is directly proportional to d [Eq. (A7) in the Appendix]. As d increases, first generation backscattered electrons spread farther away from the focal spot, and fewer of them reenter the hatched area of the anode seen in Fig. 1(b). Consequently, fewer of the higher generations are produced, and the values of η_2 and $\eta_{>2}$ are reduced. The angular distributions in Fig. 5(b) do not change appreciably with d, but the energy spectra of second and higher generations in Fig. 3(b) shift towards lower energies. At the patient plane, the off-focal component is reduced as d increases because geometric constraints prevent many of the widely spread off-focal x rays from reaching the patient plane. As a numerical example, for the representative diagnostic system described in Sec. II C with no added filtration, when d is increased from 1.5 to 3.0 cm for a fixed kVp of 100, simulation results show that η_2 and $\eta_{>2}$ in Table I reduce from 18.1% and 13.8% to 8.8%, and 3.4%, respectively. At the patient plane, the values of $\Delta K_{\text{air}}/(K_{\text{air}})_{\text{primary}}$, $\Delta\text{HVL}/(\text{HVL})_{\text{primary}}$, and $\Delta E_{\text{eff}}/(E_{\text{eff}})_{\text{primary}}$ change from +8.0%, −1.5%, and −4.0% [Fig. 11(a)] to +1.5%, −0.3%, and −0.8%, respectively. This shows that the off-focal component is sensitive to the interelectrode distance d, or alternatively, to the electric field strength.

Our simulations so far have been done for anode disks made of the same material as the focal tracks. For a tungsten/rhenium track and a molybdenum disk, our simulations (not shown) show that the extent of softening of the primary tungsten spectrum by the off-focal molybdenum spectrum is similar to that shown in Fig. 8. For tubes with a strong off-focal component, hints of the molybdenum characteristic peaks can be seen in the overall spectrum. The rest of the arguments presented throughout this study are equally valid.

The magnitude of the off-focal component is expected to be smaller for larger focal spot sizes mainly because some of the backscattered electrons will reenter the anode *within* the focal spot and the x rays they generate would not contribute to the off-focal component. Typical focal spot sizes can be as large as $2\times 2\,\text{mm}^2$. For the representative diagnostic system described in Sec. II C, this corresponds to an area of $2/\sin 16° = 7.3\times 2\,\text{mm}^2$ of the anode surface hit by primary electrons, which is equivalent to a circle of radius 2.2 mm. From Fig. 6(a), the area under the diagnostic tube curve for $R' \in [0, 0.22]$ is only 1.5% of the area under the entire curve. This shows that the fraction of backscattered electrons that reenter the anode *within* the focal spot is negligible for typical focal spot sizes. Consequently, the results presented in this study for point-like focal spots are equally valid for typical finite-size focal spots.

Recently, good agreement has been reported in the literature between simulation results using EGSnrc/BEAMnrc and experimental measurements of half-value layers[44] and x-ray spectra[48] when the off-focal component was *not* included in the simulations. Based on the arguments presented above, this can be explained as follows. The setup in Mainegra-Hing and Kawrakow[44] includes pinhole geometry and heavy composite (aluminum+copper) filtration, both of which we have shown to strongly reduce the effect of the off-focal component on the HVL [Fig. 11(b)]. We confirmed this by resimulating the NRC x-ray tube they used, and the half-value layers with and without the off-focal component were the same within <1%. The setup in Bazalova and Verhaegen[48] in-

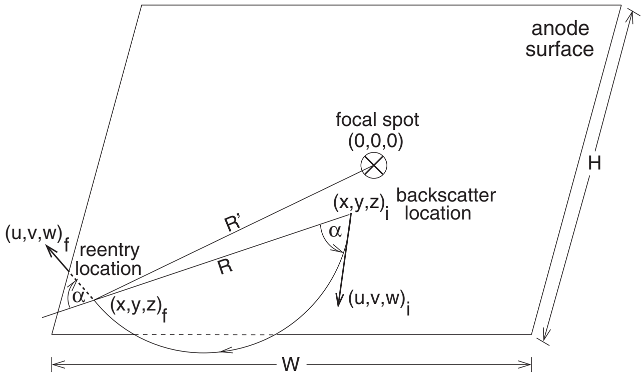

FIG. 12. (Not to scale) Definition of the parameters describing the motion of electrons backscattering from an anode surface. W and H are originally defined in Fig. 1.

cludes a 90°-Compton scatterer with narrow collimation. Such configuration also eliminates the effect of the off-focal component on the spectral shapes. In addition, the type of grounding and the tube design specifications strongly affect the extent of the off-focal component as discussed above.

IV. CONCLUSIONS

A new feature has been added to BEAMnrc to simulate off-focal radiation and excellent agreement with experimental measurements has been obtained for both the primary and the off-focal components. The study concludes that the off-focal component due to electrons that backscatter from the anode can have non-negligible effects on the output of an x-ray tube simulation, including the spectral shape, the air kerma at the patient plane per incident primary electron, the half-value layer, and the effective energy of the spectrum. The effects are larger for grounded cathode tubes, smaller interelectrode distance, higher tube voltage, lighter filtration, and less collimation. This study recommends including the off-focal component in x-ray tube simulations for more realistic modeling of these systems.

ACKNOWLEDGMENTS

The authors are grateful to Drs. Paul Johns, Tong Xu, John Boone, and Anthony Seibert for valuable discussions on the subject. Thanks to Blake Walter of NRC for the extensions made to BEAMnrc as a result of this study. The comments on the manuscript from our Carleton colleagues: Randy Taylor, Dan La Russa, Lilie Wang, and Rowan Thomson are appreciated and were very useful. This work is partially funded by the Natural Sciences and Engineering Research Council of Canada (NSERC), the Canada Research Chairs program (CRC), the Canada Foundation for Innovation (CFI), and the Ontario Innovation Trust (OIT).

APPENDIX: ALGORITHM ADDED TO BEAMnrc TO SIMULATE OFF-FOCAL RADIATION

Consider a pencil beam of electrons incident on an anode surface at the focal spot (0,0,0), as shown in Fig. 12. The total energy of an incident electron is $\varepsilon_0 = E_0 + m_0c^2$, where m_0 is the electron rest mass, c is the speed of light, and E_0 is the electron kinetic energy given by $E_0 = e$ kV where e is the absolute value of the electron charge and the kV is the applied tube voltage. Consider an electron with kinetic energy E and total energy $\varepsilon_i = E + m_0c^2$ backscattering out of the anode into the tube vacuum at (x_i, y_i, z_i) with direction cosines (u_i, v_i, w_i), which correspond to a backscattering angle α as seen in Fig. 12. Before this study was done, the interelectrode electric field was not taken into account in BEAMnrc simulations; therefore, the electrons backscattering in the tube vacuum were not properly transported and were most likely discarded. In this study, backscattered electrons are properly transported to reenter the anode under the influence of the electric field. The goal of the following algorithm is to determine the parameters of backscattered electrons upon reentering the anode, i.e., the goal of the algorithm is to obtain ε_f, (x_f, y_f, z_f) and (u_f, v_f, w_f).

For ε_f: ignoring radiation damping in the tube vacuum, as discussed in Sec. II A, means that

$$\varepsilon_f = \varepsilon_i. \tag{A1}$$

For (x_f, y_f, z_f): to determine the location of reentry (x_f, y_f, z_f), the range (R) of the backscattered electron is needed. R can be obtained by solving the relativistic equation of motion of the backscattered electron in vacuum as follows: at time t, the rate of change of the electron momentum is $\dot{\mathbf{p}} = -e\mathbf{E}_{\mathrm{field}}$, where E_{field} is the magnitude of the electric field strength given by $E_{\mathrm{field}} = \mathrm{kV}/d = E_0/ed$, where d is the interelectrode distance. Breaking the momentum equation into two components, one parallel and one perpendicular to the electric field, then integrating with respect to time, one gets

$$p_{\parallel} = -eE_{\mathrm{field}}t + p_{i_{\parallel}} \quad \text{and} \quad p_{\perp} = p_{i_{\perp}}. \tag{A2}$$

At time t, the total energy (ε) of the backscattered electron is then

$$\varepsilon = \sqrt{m_0^2c^4 + p^2c^2} = \sqrt{e^2c^2E_{\mathrm{field}}^2t^2 - 2ec^2p_{i_{\parallel}}E_{\mathrm{field}}t + \varepsilon_i^2}. \tag{A3}$$

The momentum components and the total energy of the backscattered electron can be used to express its velocity $(v_{\parallel}, v_{\perp})$ and position $(s_{\parallel}, s_{\perp})$ components as:

$$v_{\parallel} = ds_{\parallel}/dt = p_{\parallel}c^2/\varepsilon \quad \text{and} \quad v_{\perp} = ds_{\perp}/dt = p_{\perp}c^2/\varepsilon. \tag{A4}$$

Substituting Eqs. (A2) and (A3) into Eq. (A4) and integrating with respect to time, the following two parametric equations for the backscattered electron trajectory can be obtained:

$$s_{\parallel} = \frac{1}{eE_{\mathrm{field}}}\left[\varepsilon_i - \sqrt{e^2c^2E_{\mathrm{field}}^2t^2 - 2ec^2p_{i_{\parallel}}E_{\mathrm{field}}t + \varepsilon_i^2}\ \right], \tag{A5}$$

$$s_{\perp} = \frac{p_{i_{\perp}} c}{eE_{\text{field}}} \left[\sinh^{-1}\left(\frac{p_{i_{\parallel}} c}{\sqrt{\varepsilon_i^2 - p_{i_{\parallel}}^2 c^2}} \right) - \sinh^{-1}\left(\frac{p_{i_{\parallel}} c - ecE_{\text{field}} t}{\sqrt{\varepsilon_i^2 - p_{i_{\parallel}}^2 c^2}} \right) \right]. \quad \text{(A6)}$$

When t is eliminated from Eqs. (A5) and (A6), it can be shown that the result is identical to the equation given without proof by Bielajew[36] for the electron trajectory. At the point where the backscattered electron reenters the anode, $s_{\parallel}=0$ and $s_{\perp}=(s_{\perp})_{\max}=R$. Using Eqs. (A5) and (A6), with $s_{\parallel}=0$, R can be shown to be given by

$$R = \frac{\varepsilon_i d\beta_{i_{\perp}}}{E_0} \ln\left(\frac{1+\beta_{i_{\parallel}}}{1-\beta_{i_{\parallel}}} \right), \quad \text{(A7)}$$

where $\beta=v/c$. It can be shown that for $\beta \ll 1$, Eq. (A7) reduces to its familiar nonrelativistic limit $[R=4(E/E_0)d \sin\alpha \cos\alpha]$. Once R is known, the location of reentry of the backscattered electron (x_f,y_f,z_f) can be determined using:

$$x_f = x_i + L_1 R, \quad y_f = y_i + L_2 R, \quad z_f = z_i + L_3 R = -x_f \cot\theta, \quad \text{(A8)}$$

where (L_1,L_2,L_3) are the direction cosines of the vector pointing from the backscatter location to the reentry location. Using analytic geometry,[49] (L_1,L_2,L_3) can be shown to be given in terms of the original direction cosines (u_i,v_i,w_i) and the anode tilt angle θ (shown in Fig. 1) as:

$$L_1 = (u_i \sin\theta - w_i \cos\theta)\sin\theta \;/\; \sqrt{v_i^2 + (u_i \sin\theta - w_i\cos\theta)^2},$$
$$L_2 = v_i / \sqrt{v_i^2 + (u_i \sin\theta - w_i\cos\theta)^2}, \quad \text{(A9)}$$
$$L_3 = -L_1 \cot\theta.$$

If the calculated (x_f,y_f,z_f) lie outside the anode area of width W and height H, i.e., the area equivalent to the hatched area in Fig. 1(b) (see Sec. II A for a full discussion), then the backscattered electron is discarded. Otherwise, the algorithm proceeds to calculate (u_f,v_f,w_f).

For (u_f,v_f,w_f): in the plane of motion of the backscattered electron, the reentry angle is the same as the backscatter angle (both are α). However, (u_f,v_f,w_f) are different from (u_i,v_i,w_i) because of the tilt angle of the anode (θ). Using analytic geometry, (u_f,v_f,w_f) can be shown to be given in terms of the original direction cosines (u_i,v_i,w_i), the anode tilt angle (θ) and the backscatter angle (α) as:

$$u_f = L_1 \cos\alpha - \cos\theta \sin\alpha, \quad v_f = v_i,$$
$$w_f = L_3 \cos\alpha - \sin\theta\sin\alpha. \quad \text{(A10)}$$

The result $v_f=v_i$ is expected because the anode surface contains the Y axis as shown in Fig. 1(b). Another check is that for a hypothetical vertical anode $(\theta=0)$, when an electron backscatters in the XZ plane, i.e., no Y component of the velocity and $v_i=0$, one gets $L_1=0$ and $L_3=1$, which gives $u_f=-\sin\alpha$, $v_f=0$, and $w_f=\cos\alpha$, again as expected.

Equations (A1), (A8), and (A10) determine the parameters needed in the BEAMnrc simulation when the backscattered electron reenters the anode.

[a]Electronic mail: eali@physics.carleton.ca
[b]Electronic mail: drogers@physics.carleton.ca; www: http://www.physics.carleton.ca/~drogers/

[1]H. E. Johns and J. R. Cunningham, *The Physics of Radiology*, 4th ed. (Charles C. Thomas, Springfield, Illinois, 1983), pp. 592–593.
[2]W. W. Nicholas, "X-ray isochromats of copper taken in different directions relative to the cathode stream," Phys. Rev. **29**, 619631 (1927).
[3]W. W. Nicholas, "Continuous spectrum x rays from thin targets," J. Res. Natl. Bur. Stand. **2**, 837–870 (1929).
[4]L. Mallet and R. Maurin, "A study of quality and origin of parasitic radiation from the target of an x-ray tube," Radiology **48**, 628–632 (1947).
[5]H. Kuhn and H. Gajewski, "The extra-focal radiation from rotating anode x-ray tubes and its effect on the quality of the radiograph," Electromedica **4**, 125–130 (1971).
[6]R. Birch, "The spectrum and intensity of extra-focal (off-focus) radiation," Br. J. Radiol. **49**, 951–955 (1976).
[7]G. M. Ardran and H. E. Crooks, "Penetrameter cassette calibration to 400 kV and effects of extra-focal radiation when measuring tube filtration," Br. J. Radiol. **51**, 29–34 (1978).
[8]R. Thoraeus, "The amount of off-focus radiation in beams from various types of Roentgen tubes," Acta Radiol. **18**, 753–760 (1937).
[9]K. Shiga and M. Yoshida, "Methods of eliminating off-focus x-rays in rotating-anode x-ray tubes," Toshiba Review 41–48, Winter (1963).
[10]W. W. Roeck, J. T. Martin, and R. Beach, "Analysis of contributing factors to the occurrence of off-focus radiation (OFR)," Med. Phys. **19**, 1201–1204 (1992).
[11]M. Braun, "Focal spots in the future of mammography," *Reduced-Dose Mammography: Proc. 2nd Reduced-Dose Mammography Meeting*, edited by W. W. Logan and E. P. Muntz, (Masson Publishing, New York, 1979), pp. 195–209.
[12]W. W. Roeck, "X-ray source assembly acceptance testing," *Specifications, Acceptance Testing and Quality Control of Diagnostic X-ray Imaging Equipment, Medical Physics Monograph No. 20*, edited by J. A. Seibert, G. T. Barnes, and R. G. Gould (AAPM, New York, 1994), pp. 205–231.
[13]O. Mattsson, "Some factors which influence the quality of the radiographic image," Acta Radiol., Suppl. **120**, 147–206 (1955).
[14]G. M. Ardran, H. E. Crooks, and B. J. O'Loughlin, "The speed of systems and image quality," *The Reduction of Patient Dose by Diagnostic Radiologic Instrument*, edited by R. D. Moseley and J. H. Rust, Charles C. Thomas Publishers, Springfield, Illinois, 1964, pp. 222–233.
[15]G. Rao, "Influence of off-focal radiation on radiographic resolution and patient exposure," Appl. Radiol. 45–49, May/June (1974).
[16]K. E. Weaver, M. S. Robert, and F. Wagner, "Performance considerations of x-ray tube focal spot," SPIE—Medical X-Ray Photo-Optical Systems Evaluation **56**, 150–158 (1975).
[17]H. D. Nagel, "Limitations in the determination of total filtration of x-ray tube assemblies," Phys. Med. Biol. **33**, 271–289 (1988).
[18]C. A. Carlsson, "Differences in reported backscatter factors for low-energy x-rays: A literature study," Phys. Med. Biol. **38**, 521–531 (1993).
[19]E. Gabbay, "X-ray source assembly design," *Specifications, Acceptance Testing and Quality Control of Diagnostic X-ray Imaging Equipment, Medical Physics Monograph No. 20*, edited by J. A. Seibert, G. T. Barnes, and R. G. Gould (AAPM, New York, 1994), pp. 173–204.
[20]Z. Wen, R. Fahrig, S. Conolly, and N. J. Pelc, "Investigation of electron trajectories of an x-ray tube in magnetic fields of MR scanners," Med. Phys. **34**, 2048–2058 (2007).
[21]Z. Wen, N. J. Pelc, W. R. Nelson, and R. Fahrig, "Study of increased radiation when an x-ray tube is placed in a strong magnetic field," Med. Phys. **34**, 408–418 (2007).
[22]S. Z. Shen, A. K. Bloomquist, G. E. Mawdsley, and M. J. Yaffe, "Effect of scatter and an antiscatter grid on the performance of a slot-scanning digital mammography system," Med. Phys. **33**, 1108–1115 (2006).
[23]W. Jackson, "Measurement of the kilovoltage by the penetrameter—Theoretical aspects," Phys. Med. Biol. **20**, 268–281 (1975).

[24]G. V. Pavlinsky and A. Y. Portnoy, "Calculating the spectral distribution of x-ray tubes with grounded cathode," Radiat. Phys. Chem. **62**, 207–213 (2001).
[25]G. V. Pavlinsky and A. Y. Portnoy, "Formation features of radiation from x-ray tubes with grounded cathode," X-Ray Spectrom. **31**, 247–251 (2002).
[26]D. W. O. Rogers, B. A. Faddegon, G. X. Ding, C.-M. Ma, J. Wei, and T. R. Mackie, "BEAM: A Monte Carlo code to simulate radiotherapy treatment units," Med. Phys. **22**, 503–524 (1995).
[27]D. W. O. Rogers, B. Walters, and I. Kawrakow, BEAMnrc Users Manual, NRC Technical Report PIRS-509(A) rev K, National Research Council of Canada, Ottawa, Canada, http://www.irs.inms.nrc.ca/BEAM/beamhome.html (2007).
[28]I. Kawrakow, "Accurate condensed history Monte Carlo simulation of electron transport. I. EGSnrc, the new EGS4 version," Med. Phys. **27**, 485–498 (2000).
[29]I. Kawrakow and D. W. O. Rogers, The EGSnrc Code System: Monte Carlo simulation of electron and photon transport, NRC Technical Report PIRS-701 v4-2-2-5, National Research Council of Canada, Ottawa, Canada, http://www.irs.inms.nrc.ca/inms/irs/EGSnrc/EGSnrc.html (2007).
[30]E. S. M. Ali and D. W. O. Rogers, "Benchmarking EGSnrc in the kilovoltage energy range against experimental measurements of charged particle backscatter coefficients," Phys. Med. Biol. **53**, 1527–1543 (2008).
[31]E. S. M. Ali and D. W. O. Rogers, "Energy spectra and angular distributions of charged particles backscattered from solid targets," J. Phys. D **41**, 055505 (9pp) (2008).
[32]D. J. Griffiths, *Introduction to Electrodynamics* (Prentice Hall, Upper Saddle River, New Jersey, 1999), p. 286.
[33]H. Bittorf, *Imaging Systems for Medical Diagnostics*, edited by E. Krestel (Siemens AG, Berlin, 1990), p. 234.
[34]T. C. Bradbury, *Theoretical Mechanics* (John Wiley, New York, 1968), pp. 271–273.
[35]J. Rodney and M. Vaughan, "Electron flow in the conventional x-ray tube," IEEE Trans. Electron Devices **32**, 654–657 (1985).
[36]A. F. Bielajew, "Electron transport in $\vec{E}$ and $\vec{B}$ fields," *Monte Carlo Transport of Electrons and Photons*, edited by T. M. Jenkins, W. R. Nelson, A. Rindi, A. E. Nahum, and D. W. O. Rogers (Plenum Press, New York, 1988), pp. 421–434.
[37]W. R. Nelson, H. Hirayama, and D. W. O. Rogers, The EGS4 code system, Report No. SLAC-265, Stanford Linear Accelerator Center, Stanford, California, 1985.
[38]M. M. Tesic, M. F. Piccaro, and B. Munier, "Full field digital mammography scanner," Eur. J. Radiol. **31**, 2–17 (1997).
[39]G. M. Besson, A. Koch, M. Tesic, R. Sottoriva, P. Prieur-Drevron, B. Munier, E. Calais, and P. DeGroot, "Design and evaluation of a slot-scanning full-field digital mammography system," *Proc. SPIE 4682*, edited by L. E. Antonuk and M. J. Yaffe, pp. 457–468, 2002.
[40]S. M. Seltzer and M. J. Berger, "Bremsstrahlung spectra from electron interactions with screened atomic nuclei and orbital electrons," Nucl. Instrum. Methods Phys. Res. B **12**, 95–134 (1985).
[41]S. M. Seltzer and M. J. Berger, "Bremsstrahlung energy spectra from electrons with kinetic energy from 1 keV to 10 GeV incident on screened nuclei and orbital electrons of neutral atoms with $Z=1-100$," At. Data Nucl. Data Tables **35**, 345–418 (1986).
[42]M. J. Berger and J. H. Hubbell, XCOM: Photon Cross Sections on a Personal Computer, Report No. NBSIR87–3597, National Institute of Standards and Technology (NIST), Gaithersburg, Maryland, 1987.
[43]I. Kawrakow, D. W. O. Rogers, and B. Walters, "Large efficiency improvements in BEAMnrc using directional Bremsstrahlung splitting," Med. Phys. **31**, 2883–2898 (2004).
[44]E. Mainegra-Hing and I. Kawrakow, "Efficient x-ray tube simulations," Med. Phys. **33**, 2683–2690 (2006).
[45]E. S. M. Ali and D. W. O. Rogers, "Efficiency improvements of x-ray simulations in EGSnrc user-codes using Bremsstrahlung cross section enhancement (BCSE)," Med. Phys. **34**, 2143–2154 (2007).
[46]R. F. Wagner, K. E. Weaver, E. W. Denny, and R. G. Bostrom, "Towards a unified view of radiological imaging systems—Part I: Noiseless images," Med. Phys. **1**, 11–24 (1974).
[47]K. Cranley, B. J. Gilmore, G. W. Fogarty, and L. Desponds, Catalogue of diagnostic x-ray spectra and other data—CD edition (electronic version prepared by D Sutton), Technical Report No. 78, The Institute of Physics and Engineering in Medicine (IPEM), 1997.
[48]M. Bazalova and F. Verhaegen, "Monte Carlo simulation of a computed tomography x-ray tube," Phys. Med. Biol. **52**, 5945–5955 (2007).
[49]G. Salmon, *A Treatise on the Analytic Geometry of Three Dimensions*, Vol. I, 7th ed. (Chelsea Publishing Co., New York, 1965).